

# Probing the Dynamics of the Metallic-to-Semiconducting Structural Phase Transformation in MoS<sub>2</sub> Crystals

Yinsheng Guo,<sup>†</sup> Dezheng Sun,<sup>‡,#</sup> Bin Ouyang,<sup>§,#</sup> Archana Raja,<sup>†</sup> Jun Song,<sup>§</sup> Tony F. Heinz,<sup>‡,⊥</sup> and Louis E. Brus<sup>\*,†</sup>

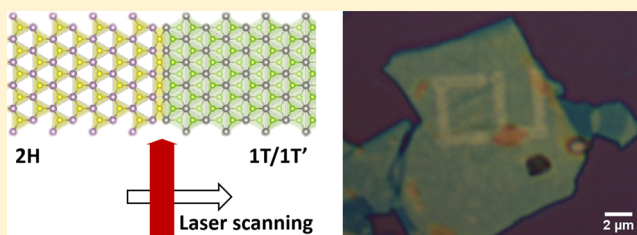
<sup>†</sup>Department of Chemistry and <sup>‡</sup>Department of Physics, Columbia University, New York, New York 10027, United States

<sup>§</sup>Mining and Materials Engineering, McGill University, Montreal, QC H3A 0C5, Canada

## S Supporting Information

**ABSTRACT:** We have investigated the phase transformation of bulk MoS<sub>2</sub> crystals from the metastable metallic 1T/1T' phase to the thermodynamically stable semiconducting 2H phase. The metastable 1T/1T' material was prepared by Li intercalation and deintercalation. The thermally driven kinetics of the phase transformation were studied with *in situ* Raman and optical reflection spectroscopies and yield an activation energy of 400 ± 60 meV (38 ± 6 kJ/mol). We calculate the expected minimum energy pathways for these transformations using DFT methods. The experimental activation energy corresponds approximately to the theoretical barrier for a single formula unit, suggesting that nucleation of the phase transformation is quite local. We also report that femtosecond laser writing converts 1T/1T' to 2H in a single laser pass. The mechanisms for the phase transformation are discussed.

**KEYWORDS:** Molybdenum disulfide, structural phase transition, energy barrier, Raman spectroscopy, laser patterning



MoS<sub>2</sub> is a member of the transition metal dichalcogenide (TMD) family.<sup>1</sup> This family consists of two-dimensional planar sheets that stack via weak van der Waals interlayer interactions. MoS<sub>2</sub> exhibits several different polymorphs. The thermodynamically stable phase is semiconducting 2H MoS<sub>2</sub>, in which each molybdenum atom is coordinated by six sulfur atoms in a trigonal prismatic geometry. The metallic 1T/1T' phase of MoS<sub>2</sub> differs from 2H MoS<sub>2</sub> in that the coordination of Mo by S atoms is octahedral (twisted octahedral in the 1T' variant). Octahedral 1T/1T' MoS<sub>2</sub> spontaneously forms under Li intercalation; this process has been extensively modeled.<sup>2–6</sup> Most remarkably, subsequent deintercalation preserves octahedral coordination, yielding a metastable 1T/1T' metallic phase of MoS<sub>2</sub>.<sup>7</sup>

MoS<sub>2</sub> has generated intense interest recently with promising applications in tribology, hydrodesulfurization catalysis,<sup>8</sup> photocatalysis,<sup>9</sup> and electrocatalysis.<sup>10–13</sup> In 2H MoS<sub>2</sub>, the edge site sulfur atoms are responsible for catalytic activity, whereas the basal plane is inactive.<sup>14</sup> In contrast, the metallic 1T/1T' phase has been shown to be catalytically active in the whole basal plane.<sup>15,16</sup> Recently, a coherent in-plane heterostructure between the semiconducting 2H and metallic 1T/1T' phases was induced by electron bombardment of single-layer MoS<sub>2</sub> and was studied using scanning transmission electron microscopy (STEM).<sup>17,18</sup> Such 2D heterostructures open up new possibilities in basic research and device applications.<sup>19</sup>

Scanning tunneling microscopy<sup>20</sup> and Raman spectroscopy<sup>21</sup> studies have, however, shown that the bulk 1T/1T' phase is metastable under ambient conditions. The octahedral coordinated 1T/1T' structure converts to trigonal prismatic

coordinated 2H structure during room temperature aging or thermal annealing. Understanding the thermodynamics and kinetics of this structural transformation is thus critical in order to realize the application potential of the metastable 1T/1T' MoS<sub>2</sub>. While the structure and properties of the MoS<sub>2</sub> polymorphs have been extensively investigated, experimental studies of the 1T/1T' to 2H structural transformation kinetics are still lacking. Here we report a measurement of the activation energy of the structural transformation from the 1T/1T' phase to the 2H phase. We employ *in situ* Raman spectroscopy to measure the reaction rate and monitor the local temperature. We also demonstrate that direct femtosecond laser writing can serve as a new method for patterning MoS<sub>2</sub> heterostructures.

**Experimental and Theoretical Methods.** Thin samples of MoS<sub>2</sub> for our study were prepared by a cycle of Li intercalation and deintercalation. To this end, MoS<sub>2</sub> crystals, typically about tens of nanometers thick and tens of microns in lateral size, were mechanically exfoliated from natural MoS<sub>2</sub> crystals (SPI) on a Si substrate with a 285 nm thermal oxide layer. Prior to exfoliation, the Si substrate was cleaned with piranha solution and washed with purified water. Li intercalation was performed in an Ar-filled glovebox, by immersing the MoS<sub>2</sub> sample overnight in 1.6 M *n*-butyllithium hexane solution (Sigma-Aldrich).<sup>22</sup> The O<sub>2</sub> and H<sub>2</sub>O levels inside the glovebox were below 1 ppm. The lithiated sample

Received: March 27, 2015

Revised: July 1, 2015

Published: July 2, 2015

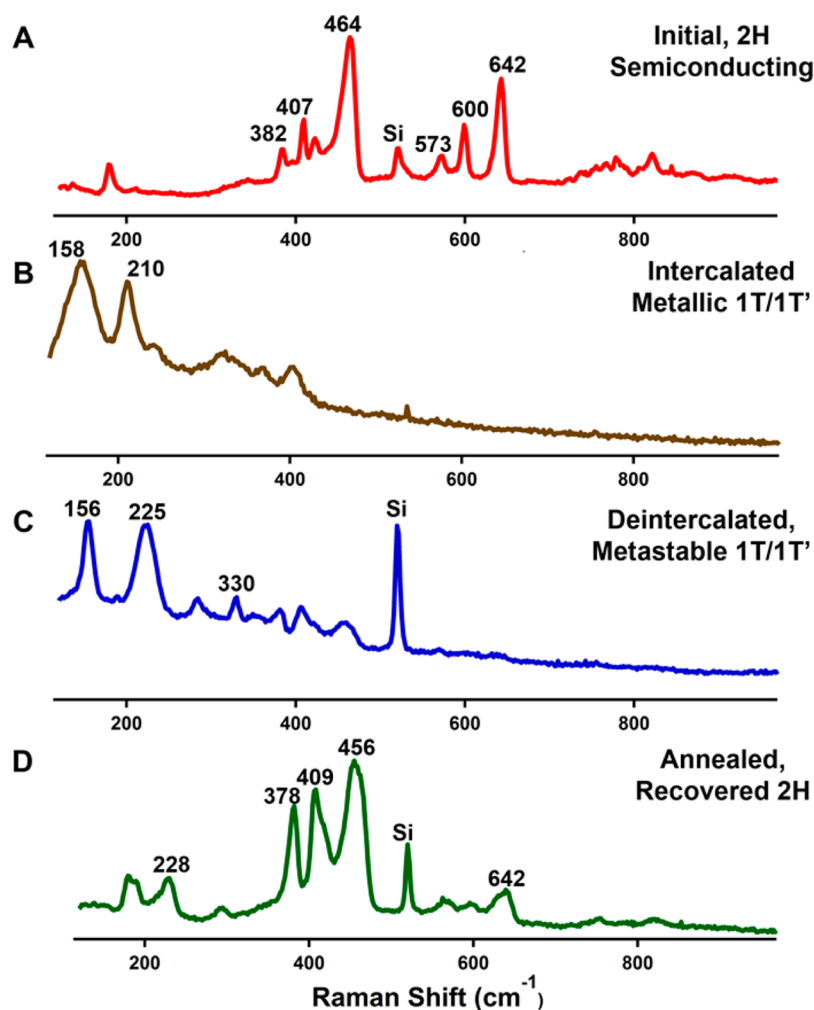


**Figure 1.** Raman spectra of MoS<sub>2</sub> polymorphs for Stokes scattering induced by weak laser excitation at 633 nm. (A) Initial 2H MoS<sub>2</sub>. (B) Li-intercalated MoS<sub>2</sub>. (C) Metastable 1T/1T' MoS<sub>2</sub> after Li deintercalation. (D) Restored 2H phase after thermal annealing of 1T/1T' sample in flowing Ar. The mode at 520 cm<sup>-1</sup> arises from the Si substrate. The absolute intensities are arbitrary; Figure S2 (Supporting Information) shows the absolute Raman intensities for the 1T/1T' and 2H phases before and after femtosecond laser annealing.

was washed in hexane and water. Gentle washing with water deintercalates Li, producing metastable 1T/1T' MoS<sub>2</sub>, as previously reported.<sup>21</sup>

*In situ* Raman spectroscopy was performed with a home-built confocal micro-Raman setup using a continuous-wave He–Ne laser operating at 633 nm. To measure the local temperature, the anti-Stokes and Stokes Raman spectra were collected sequentially, using short and long pass filters, respectively, on the same sample spot with constant laser power and alignment. The Raman spectra were calibrated with a Ne pen lamp. Spectra of the original 2H phase and the deintercalated metastable 1T/1T' phase of MoS<sub>2</sub> were taken under ambient conditions. Raman spectra of Li intercalated MoS<sub>2</sub> samples were collected in a turbo-pumped vacuum optical cryostat. The sample was first loaded into the optical cryostat, sealed in the glovebox, and mounted on the micro-Raman setup without exposure to air. Thermal annealing was carried out in a quartz tube furnace at 573 K under continuous Ar flow for 1 h.

An amplified femtosecond laser operating at a repetition rate of 1 MHz was employed in the laser writing demonstration. Pulses at a wavelength of 780 nm with a duration of ~100 fs were produced using a noncolinear optical parametric amplifier (NOPA). This radiation was coupled into a microscope and

focused by a 100× objective onto the MoS<sub>2</sub> sample. To induce the phase transformation from the metastable 1T/1T' phase, the sample was scanned at a speed of 0.01 mm/s, with a typical power of 0.15 mW

Optical reflectivity spectra were measured using a quartz-tungsten-halogen lamp as light source. A 100 μm pinhole after the lamp served as a point source and was collimated by an achromat lens. The collimated beam was focused on the sample with a 40× objective, which also collected the reflected light. The reflected light was subsequently dispersed by a spectrometer and recorded by a liquid nitrogen cooled CCD.

In the theoretical studies of the phase transformation, we made use of density functional theory (DFT).<sup>1,2</sup> The calculations employed the projector augmented wave method (PAW)<sup>3</sup> and the generalized gradient approximation (GGA)<sup>4</sup> in the Vienna *ab initio* Simulation Package (VASP).<sup>23</sup> A periodic simulation box consisting of 2 × 2 unit cells of monolayer MoS<sub>2</sub> was constructed with a spacing perpendicular to the MoS<sub>2</sub> sheet of 15 Å to eliminate interlayer interactions. An energy cutoff of 400 eV and 9 × 9 K-mesh were chosen to achieve desired accuracy. The simulation box was fully relaxed to obtain the ground state of each phase. The phase transition, occurring directly between two different ground states, was

studied using the climbing image Nudged Elastic Band (ci-NEB) method,<sup>24</sup> with a force convergence  $<0.05$  eV/Å.

**Results and Discussion. Raman and Optical Reflectivity Characterization of MoS<sub>2</sub> Polymorphs.** Raman spectroscopy provides detailed information on the structure of the MoS<sub>2</sub> crystals.<sup>25,26</sup> Figure 1 displays the spectra of pristine MoS<sub>2</sub> (2H), Li intercalated MoS<sub>2</sub> (1T/1T'), deintercalated MoS<sub>2</sub> (metastable 1T/1T'), and thermally annealed MoS<sub>2</sub> (2H) for 633 nm excitation.

The 2H Raman spectrum, produced by off-resonance 514 nm excitation, exhibits zone-center modes at  $383$  cm<sup>-1</sup> ( $E_{2g}$ ) and  $409$  ( $A_{1g}$ ) cm<sup>-1</sup>.<sup>25</sup> These modes are relatively weak in the Raman spectrum excited by 633 nm laser radiation, which is in resonance with the direct optical transition of the material at K-point. The 633 nm spectrum is dominated by higher-order features: an intense asymmetric peak at  $460$  cm<sup>-1</sup> and modes at  $572$ ,  $600$ , and  $643$  cm<sup>-1</sup>. The correct assignment and resonance mechanism of these features have been the subjects of debate.<sup>27–30</sup> Another feature of the resonant Raman spectrum of the 2H phase is the existence of a continuum background. The continuum arises from photoluminescence from resonant excitation near the direct gap of the material at the K-point of the Brillouin zone, an inefficient process in multilayer 2H MoS<sub>2</sub> because of the lower-lying indirect gap.

Our initial 2H spectrum agrees well with previously reported spectra for the bulk crystalline 2H phase, indicating the high quality of our exfoliated sample. The 1T/1T' spectra both before and after deintercalation also are consistent with previous reports: all traces of the intense features higher-frequency modes are absent in this metallic phase. In the 1T/1T' phase after deintercalation, three new modes ( $156$ ,  $225$ , and  $330$  cm<sup>-1</sup>) can be observed through a zone-folding scheme that maps M-point phonon modes onto the  $\Gamma$ -point, in agreement with previous reports.<sup>21</sup>

After furnace annealing at  $573$  K in flowing Ar, the resonant Raman features of 2H MoS<sub>2</sub> are partially restored. In annealed 2H samples, the higher-order  $460$ ,  $572$ ,  $600$ , and  $643$  cm<sup>-1</sup> features are significantly weaker, only about the same intensity as the first-order  $383$  and  $409$  cm<sup>-1</sup> modes. The line width of all peaks are broadened compared with original 2H spectrum. Also, a new  $228$  cm<sup>-1</sup> mode appears, which corresponds to the longitudinal acoustic mode at the M-point.<sup>27</sup> This mode becomes allowed by disorder, like the behavior of the D-mode peak in graphene.<sup>27</sup> These observations suggest that the resonant enhancement is weaker in the recovered 2H sample due to structural disorder and reduced domain size. Indeed, our recovered 2H spectrum is similar to the resonant spectrum of  $20$  nm diameter 2H MoS<sub>2</sub> nanoparticles, as reported by Frey et al.<sup>27</sup> The MoS<sub>2</sub> layers are severely distorted into a fullerene-like geometry in these onion-like nanoparticles.

Figure 2 shows the optical reflectance spectra of pristine 2H MoS<sub>2</sub> and lithiated 1T/1T' MoS<sub>2</sub>. The 2H phase exhibits excitonic features in the reflectance where the photon energy matches the direct transitions at K-point in electronic structure of the 2H phase. The 1T/1T' phase reflectance is rather flat and featureless. The 1T/1T' phase reflectance is generally lower than 2H phase across the optical range of our measurement. These differences contribute to the visual contrast that is readily observed during our photolithography demonstration with the femtosecond pulsed laser, as reported below.

**Kinetics of the Thermally Induced Structural Phase Transformation.** Here we examine the thermal and photo-

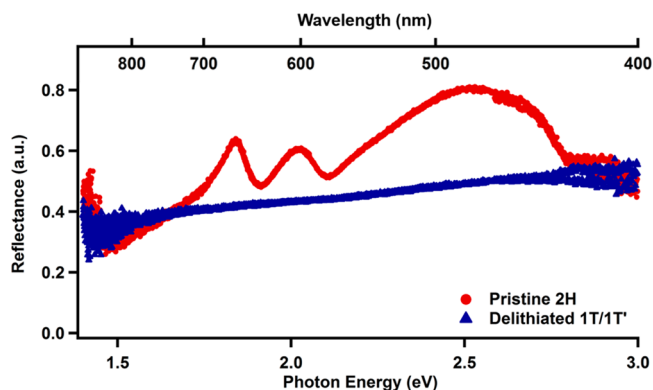


**Figure 2.** Optical reflectance spectra of pristine 2H and delithiated 1T/1T' bulk MoS<sub>2</sub> samples on quartz substrates. The 2H phase shows excitonic features. The 1T/1T' phase shows a flat spectral profile. Generally the 1T/1T' phase is less reflective than 2H, although some sample-to-sample variation is observed.

induced kinetics of the phase transformation from the metastable 1T/1T' to the equilibrium 2H phase of MoS<sub>2</sub>; the distinct Raman modes are used to report the local content of these two phases. In our studies, the laser excitation served both to heat the sample and to allow us to observe the Raman spectrum as it evolved in time. 2H samples of  $40$  nm thickness are expected to absorb about  $1/3$  of the incident  $633$  nm laser light (Supporting Information). At low laser powers (e.g.,  $\sim 100$   $\mu$ W), as used to characterize the different polymorphs in Figure 1, there is no significant heating and the 1T/1T' phase is stable for days. At higher power levels (e.g.,  $\sim 2$  mW), the 1T/1T' modes decrease and the 2H modes increase in time, as shown in Figure 3A. The background continuum response also grows as the transformation occurs. Both the initial and final phases absorb laser light, and the laser power controls the amount of heating.

The sample temperature  $T$  is inferred from the phonon populations, as reported by the ratio between anti-Stokes and Stokes Raman signals:

$$\frac{I_{aS}}{I_S} = C \exp\left(-\frac{\hbar\omega_{ph}}{k_B T}\right) \quad (1)$$

Here  $I_{aS}$  and  $I_S$  represent, respectively, the anti-Stokes and Stokes intensities,  $\omega_{ph}$  denotes the angular frequency of the relevant phonon, and  $C$  is a mode-specific prefactor.<sup>31</sup> To determine the constant  $C$ , as well as to correct for instrumental sensitivity factors, we make use of the usual scheme<sup>31</sup> of calibration using the measured anti-Stokes/Stokes ratio at room temperature. Figure 3B shows typical Stokes and anti-Stokes Raman spectra observed during the laser annealing experiment. In this example, the sample has been largely converted to 2H phase.

The sample temperature is highest at the center of the laser focal spot and decreases toward the periphery. We follow Herman's analysis for a Gaussian laser profile<sup>32</sup> to obtain the peak temperature rise from the measured anti-Stokes/Stokes Raman intensity ratio. Within the temperature range and phonon frequency used in this study, the correction is carried out according to  $\Delta T_{peak} = 2\Delta T_{uniform}$ . The actual peak temperature rise  $\Delta T_{peak}$  is twice that would be determined assuming a spatially uniform temperature distribution  $\Delta T_{uniform}$  in analyzing the experimental data.

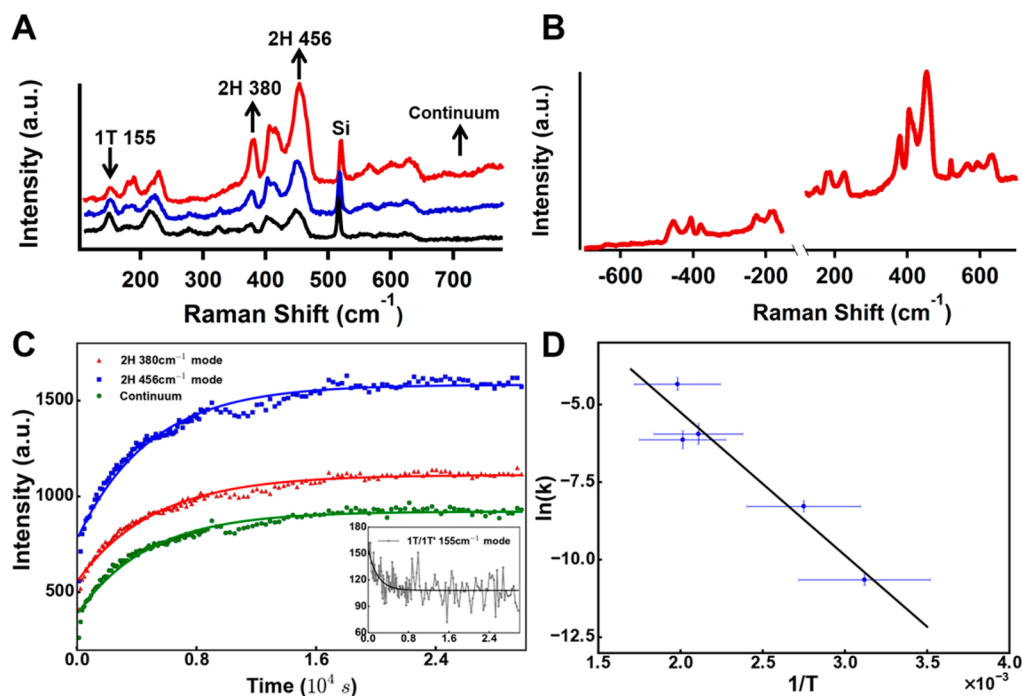


**Figure 3.** *In situ* Raman spectroscopy measurements of MoS<sub>2</sub> crystals during the 1T/1T' to 2H phase transformation. (A) Evolution of Raman spectra during 633 nm laser annealing at a calculated temperature of 364 K: initial state (black), intermediate state (blue), and final state (red). Features characteristic of the 1T/1T' phase (e.g., the 155  $\text{cm}^{-1}$  mode) decrease in intensity, while modes from the 2H phase increase in intensity. The background continuum also increases during annealing. The vertical offset has *not* been manually adjusted in these three spectra. Upward arrows indicate increasing intensity with time. The downward arrow indicates decreasing intensity with time. (B) Anti-Stokes and Stokes Raman spectra of MoS<sub>2</sub> taken after a kinetic run. Lorentzian lineshapes were used to extract Raman mode intensities, with a cubic term to describe the baseline. (C) Examples kinetics of the phase transition based on different Raman modes for annealing at 364 K and a comparison with a first-order rate law. Data are shown for the E<sub>2g</sub><sup>1</sup> at 380  $\text{cm}^{-1}$  mode, the higher-order 456  $\text{cm}^{-1}$  mode, and the background continuum. The resulting rate constants from the three fits are, respectively,  $k = 2.0 \times 10^{-4}/\text{s}$ ,  $2.1 \times 10^{-4}/\text{s}$ , and  $2.5 \times 10^{-4}/\text{s}$ . The inset shows 1T/1T' phase spectral evolution of the 155  $\text{cm}^{-1}$  mode. The rate constant extracted from the fitting is  $5.5 \times 10^{-4}/\text{s}$ , with an uncertainty of  $5.0 \times 10^{-4}/\text{s}$ . (D) Arrhenius plot for the rate of the 1T/1T' to 2H MoS<sub>2</sub> structural phase transformation. The slope yields an activation energy of  $400 \pm 60$  meV ( $38 \pm 6$  kJ/mol).

Although the laser annealing experiments were performed under ambient conditions, no evidence for the formation of oxides<sup>33</sup> (such as MoO<sub>3</sub>) was detected in the Raman spectra for either cw laser heating or the femtosecond laser writing described below. Systematic oxidation of bulk MoS<sub>2</sub> is reported to begin above 870 K.<sup>34</sup> Surface etching pits develop on MoS<sub>2</sub> above 610 K in oxygen.<sup>33</sup> In our cw laser heating measurements, the highest temperature we employed was about 500 K. AFM measurements exhibited flat surfaces, without evidence of oxidative etching. Also note that the Si substrate phonon line at about 520  $\text{cm}^{-1}$  is strong in our spectra, indicating that the laser is substantially transmitted through our MoS<sub>2</sub> samples (typically  $\sim 40$  nm thick), as discussed in the Supporting Information Section E. We are thus observing primarily the interior layers of the MoS<sub>2</sub> crystal in our Raman spectra.

In Figure 3C we present Raman data tracking the temporal evolution 1T/1T' to 2H phase transformation under laser heating. Results are shown for the emergence of different Raman features characteristic of the 2H phase. We see that the data can be fit well to first-order kinetics, from which we obtain a rate constant for each choice of Raman mode. A rate constant of  $k = 2.2 \times 10^{-4}/\text{s}$  is consistent with the different measurements within our fitting uncertainty of  $5 \times 10^{-5}/\text{s}$ . One can also follow the phase transformation by tracking the disappearance of the modes associated with the 1T/1T' phase. The inset of Figure 3C shows that kinetics obtained in this fashion agree with the kinetics based on the emergence of the

2H Raman modes within a factor of 2. The large uncertainty arises from the comparative weakness of these modes and the corresponding noise in the kinetic data. For this reason, we focus on emerging 2H phase features in our quantitative analysis of the phase transformation.

We have repeated this procedure for different laser powers to obtain the annealing rate as a function of sample temperature. Over the limited available dynamic range (Figure 3D), we can fit the temperature dependence of the rate of the phase transformation to an Arrhenius expression with an activation energy of  $400 \pm 60$  meV ( $38 \pm 6$  kJ/mol). This analysis implies that the MoS<sub>2</sub> in the 1T/1T' phase has a half-life of about 10 days at room temperature and about 5 h at 400 K. The inferred activation energy is low compared to a similar phase change reported for exfoliated–restacked WS<sub>2</sub>.<sup>35</sup> Quantitative understanding of this moderate energy barrier is of fundamental importance in the design and utilization of the metallic polymorphs of MoS<sub>2</sub> and other members of the TMD family.

**Theoretical Modeling of the Phase Transformation: Nucleation and the Transition State.** We have considered theoretically the minimum energy pathways (MEPs) for transformation between the metallic and semiconducting phases. Figure 4 presents results for the 1T  $\rightarrow$  2H and 1T'  $\rightarrow$  2H phase transformations, with the lattice configurations for the initial and final states, and the saddle points shown schematically. The 1T  $\rightarrow$  2H transformation is achieved by translating one layer of S atoms with respect to the rest of the

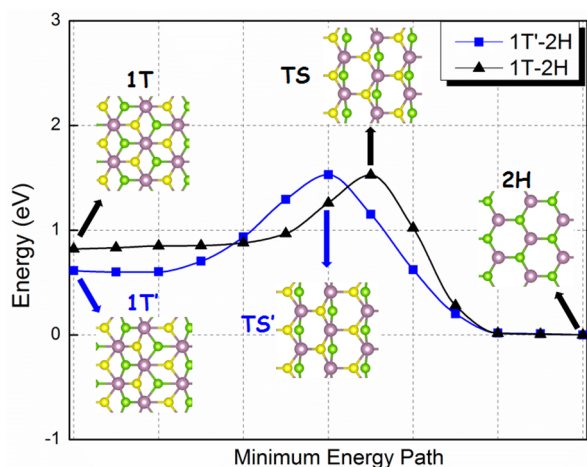


**Figure 4.** Minimum energy paths (MEPs) for  $1T \rightarrow 2H$  and  $1T' \rightarrow 2H$  phase transformations, indicated by black triangles and blue squares, respectively, with lines connecting the symbols as a guide to the eye. The structural models show the lattice configurations of the system at different stages of the phase transformation. The Mo atoms are purple, and the top and bottom layers of S atoms are green and yellow, respectively. TS and TS' denote the *transition state* at the saddle point for the respective  $1T \rightarrow 2H$  and  $1T' \rightarrow 2H$  phase transformation.

crystal. Similarly, the  $1T' \rightarrow 2H$  phase transformation also involves the translation of a plane of S atoms, but with additional displacements of Mo atoms to transform the twisted octahedra to a perfect trigonal prismatic geometry. The corresponding activation energies are computed to be 680

and 900 meV per formula unit, respectively, for  $1T \rightarrow 2H$  and  $1T' \rightarrow 2H$  transformations.

In the theory of nucleation for solid–solid phase transformations, the activation energy increases with the number of formula units in the critical nucleus (adjusted for surface/interface energies).<sup>24,36</sup> A small nanocrystal may fluctuate as a single coherent unit. In large crystalline systems, one region (critical nucleus) may coherently fluctuate, followed by phase propagation across the remaining crystal. In 3D solids with rigid bonding, the critical nucleus invariably contains many formula units, and the predicted activation energy is quite large. In real 3D crystals, solid–solid phase transitions are thought to be caused by pre-existing defects or domain structure that provide nucleation sites. A large single crystal often breaks into many small fragments upon phase transformation.

We observe an activation energy for the  $1T/1T'$  to  $2H$  process in 2D  $\text{MoS}_2$  that is remarkably low, somewhat less than the calculated values for a single formula unit. This indicates that the nucleation process is quite local and not coherent over many unit cells. The degraded  $2H$  Raman spectra observed above after annealing the delithiated  $1T/1T'$  samples indicates that the final sample is disordered. Our initial  $2H$  is quite crystalline. In general, the quality of  $1T/1T'$  samples undoubtedly depends upon the details of the intercalation/oxidation chemical process: Eda et al. report that single  $\text{MoS}_2$  layers made by colloidal chemical exfoliation of bulk  $2H$   $\text{MoS}_2$  at room temperature contain regions of all three phases:  $2H$ ,  $1T$  and  $1T'$ , with vacancy defects.<sup>17</sup> An intercalation/oxidation process does not necessarily produce defective  $1T$  structure: Wypych and Schollhorn reported that highly crystalline  $1T$  powder could be made by potassium intercalation with subsequent oxidation.<sup>37</sup> Upon heating, this crystalline  $1T$

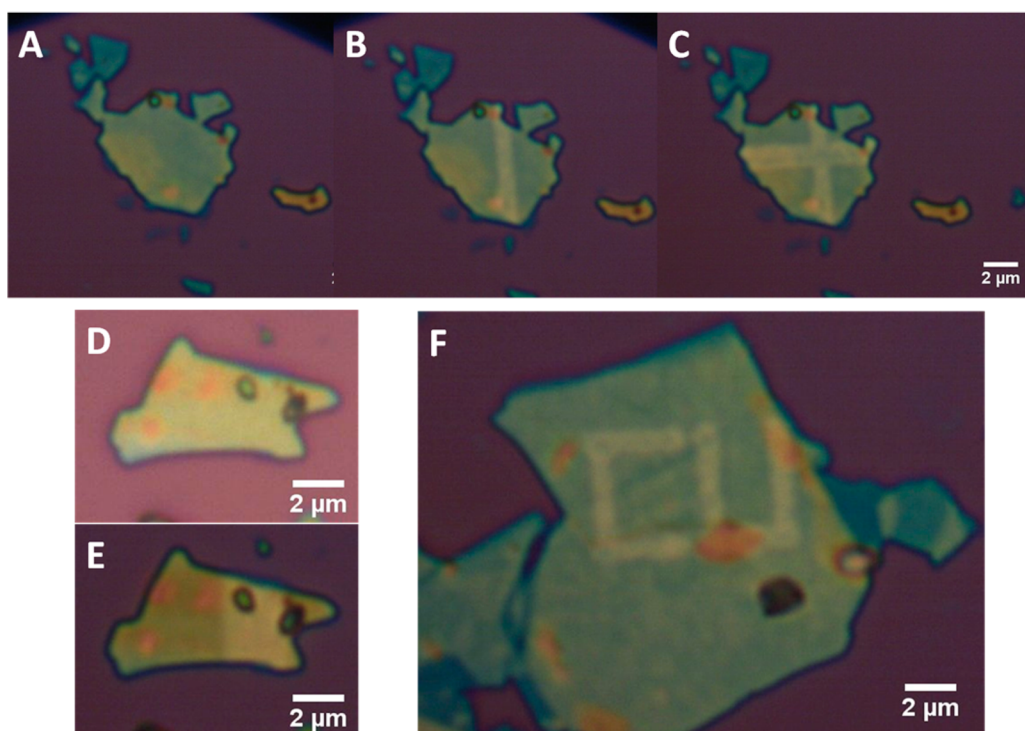


**Figure 5.** Optical micrographs of laser  $\text{MoS}_2$  samples patterned by femtosecond laser pulses. (A–C) Step-by-step snapshots of writing a ‘+’ shaped  $2H$  region in a  $1T/1T'$  flake. (D,E) Well-defined  $1T/1T'–2H$  heterojunction on a single  $\text{MoS}_2$  flake before (D) and after (E) conversion by the femtosecond laser pulses. The right half of the  $\text{MoS}_2$  flake in (E) was converted to the  $2H$  phase. (F) The letters “CU” were written on the  $\text{MoS}_2$  flake at a resolution slightly better than  $1 \mu\text{m}$ .

sample thermally converted to a 2H phase with strong rotational disorder in the X-ray powder spectra. It is not clear what to expect for nucleation theory in van der Waals materials. It may be that the gliding motion of surface atoms that occurs in the 1T–2H transition inherently leads to a small critical nucleus size. Our low activation energy indicates the existence of multiple local nucleation sites, consistent with the observations of Wypych and Schollborn, leading to a degraded 2H Raman spectrum.

**Femtosecond Laser Patterning of MoS<sub>2</sub> Structures.** A method of making MoS<sub>2</sub> samples with (arbitrarily designed) spatially varying 2H semiconducting and 1T/1T' metallic regions could be quite useful. An in-plane heterostructure in a 2D material provides a 1D interface with scientific and technological potential, as evidenced by the recently reported graphene–hexagonal boron nitride structure.<sup>38</sup> In-plane heterostructures in single-layer MoS<sub>2</sub> between 1T/1T' and 2H domains, initiated by electron bombardment of 2H, have also recently been produced.<sup>17</sup>

Here we report that femtosecond laser writing of metastable 1T/1T' MoS<sub>2</sub> can be used to fabricate such lateral heterostructures. Figure 5 shows the production of 2H regions of designed geometry from a metastable 1T/1T' crystal after a single pass of the focused ~100 fs, 780 nm, 1 MHz laser radiation, using a scan speed of 0.01 mm/s. Raman spectroscopy confirms these new areas of increased reflectivity are 2H in structure (see Supporting Information). In the figure, a 1T/1T' to 2H heterojunction spanning a single MoS<sub>2</sub> flake was fabricated with a well-defined geometry. By combining such laser-induced phase change with laser ablation, one could envisage the fabrication of a monolithic circuit consisting of semiconducting and metallic elements from a single MoS<sub>2</sub> flake/domain. This method of laser writing may be generally valuable in the transition metal dichalcogenide family, which exhibits a variety of polymorphs. We note that the short time scale for the laser-induced change with femtosecond pulses implies that lateral diffusion of the excitation will not be significant (see Supporting Information Section D). Consequently, no degradation in the spatial resolution of patterning is expected.

We note that the choice of a 780 nm wavelength for the femtosecond laser excitation is expected to lead to a self-terminating character for induction of phase transformation process in which unnecessary laser excitation is avoided. The metallic 1T/1T' phase has intraband transitions that give rise to light absorption over a broad spectral range and allow excitation by the femtosecond laser radiation. However, once the semiconducting 2H phase has been formed, the 780 nm radiation lies below the direct band gap of the material. It consequently absorbs light only weakly (See Supporting Information Section E).

In comparison with cw laser excitation, the time-averaged femtosecond laser power required to induce the phase transition greatly reduced. We are able to write structures at a scan speed of 0.01 mm/s using an average power for the femtosecond pulses of just 150 μW, which would not give rise to any meaningful annealing for cw excitation. Each femtosecond laser pulse, however, strongly excites the sample. Based on a simple heat-capacity calculation (Supporting Information), the deposited fluence by each femtosecond laser pulse (7.5 mJ/cm<sup>2</sup>) would yield an equilibrium temperature rise of the sample to ~1000 K. Despite this intense excitation, we do not observe ablation or oxidation of the sample under our experimental

conditions. However, damage and ablation is observed at a factor of 2 higher fluence (Figure S2 in the Supporting Information).

The time constant for decay of the calculated high temperature present at the end of an individual femtosecond laser pulse, by heat flow, is estimated to be of the order of 1 ns (Supporting Information). We observe the phase transformation to occur with 10<sup>5</sup> pulses, implying that the aggregate time that the sample is hot is ~10<sup>-4</sup> s. If one extrapolates the thermal conversion rate obtained at lower temperatures using cw laser heating to the high calculated temperature, the expected conversion time is about 10 s, i.e., 5 orders of magnitude longer than observed. This comparison suggests that under intense femtosecond excitation the mechanism for the phase transformation may differ from that at low temperature. The excitation within a femtosecond laser pulse is extremely energetic; we are within a factor of 2 of the damage threshold. Perhaps something similar to transient melting occurs. In addition, on the ultrashort time scale relevant for femtosecond laser excitation, strong nonequilibrium effects are expected in the material, with the electronic degree of freedom initially decoupled from the lattice. In this regime, direct electron-induced, nonthermal solid–solid phase transitions have been reported in some thin film materials.<sup>39–41</sup> These questions will be investigated in further studies.

**Conclusion.** In summary, we have induced a structural transformation in MoS<sub>2</sub> crystals from the metastable 1T/1T' phase to the equilibrium 2H phase using cw and femtosecond pulsed laser radiation. For cw heating, we have followed the kinetics with *in situ* Raman spectroscopy. The activation energy for the phase transformation inferred from the temperature dependence of kinetics is 400 ± 60 meV (38 ± 6 kJ/mol). Quantitative knowledge of this activation energy allows better understanding and control of MoS<sub>2</sub> polymorphs. We have also demonstrated direct laser writing with femtosecond laser pulses as a promising practical method to control the local crystal structure and to generate arbitrary in-plane heterostructures in MoS<sub>2</sub>.

## ■ ASSOCIATED CONTENT

### 📄 Supporting Information

Kinetics of 1T/1T' to 2H phase transformation for cw laser annealing at higher power, Raman spectra and optical images of 2H and 1T/1T' MoS<sub>2</sub> from femtosecond laser writing, temperature measurement for cw laser annealing, thermal aspects of femtosecond laser annealing, light absorption by multilayer MoS<sub>2</sub> flakes, AFM images of laser patterned MoS<sub>2</sub> samples. The Supporting Information is available free of charge on the ACS Publications website at DOI: 10.1021/acs.nanolett.5b01196.

## ■ AUTHOR INFORMATION

### Corresponding Author

\*E-mail: leb26@columbia.edu.

### Present Address

<sup>†</sup>SLAC National Accelerator Laboratory, 2575 Sand Hill Rd., Menlo Park, California 94025, United States.

### Author Contributions

<sup>#</sup>These authors contributed equally to this work. The manuscript was written through contributions of all authors. All authors have given approval to the final version of the manuscript.

## Notes

The authors declare no competing financial interest.

## ACKNOWLEDGMENTS

We thank Yilei Li, Alexey Chernikov, and Ziliang Ye for helpful discussions. This material is based upon work supported by the NSF MRSEC program through Columbia in the Center for Precision Assembly of Superstratic and Superatomic Solids (DMR-1420634), and supported by the Department of Energy, Office of Science, Basic Energy Sciences, Materials Sciences and Engineering Division, under contract DE-AC02-76SF00515, SLAC National Accelerator Laboratory, and by the National Science Foundation (grant no. DMR-1106225). The work at McGill was supported by the NSERC Discovery grant (grant # RGPIN 418469-2012) for funding resources. Computing power was provided by the Supercomputer Consortium Laval UQAM McGill and Eastern Quebec.

## REFERENCES

- (1) Chhowalla, M.; Shin, H. S.; Eda, G.; Li, L.-J.; Loh, K. P.; Zhang, H. The Chemistry of Two-Dimensional Layered Transition Metal Dichalcogenide Nanosheets. *Nat. Chem.* **2013**, *5* (4), 263–275.
- (2) Duerloo, K.-A. N.; Li, Y.; Reed, E. J. Structural Phase Transitions in Two-Dimensional Mo- and W-Dichalcogenide Monolayers. *Nat. Commun.* **2014**, *5*, 4214.
- (3) Chen, X.; Chen, Z.; Li, J. Critical Electronic Structures Controlling Phase Transitions Induced by Lithium Ion Intercalation in Molybdenum Disulfide. *Chin. Sci. Bull.* **2013**, *58* (14), 1632–1641.
- (4) Enyashin, A. N.; Seifert, G. Density-Functional Study of Li<sub>x</sub>MoS<sub>2</sub> Intercalates. *Comput. Theor. Chem.* **2012**, *999* (0), 13–20.
- (5) Wang, L.; Xu, Z.; Wang, W.; Bai, X. Atomic Mechanism of Dynamic Electrochemical Lithiation Processes of MoS<sub>2</sub> Nanosheets. *J. Am. Chem. Soc.* **2014**, *136* (18), 6693–6697.
- (6) Kan, M.; Wang, J. Y.; Li, X. W.; Zhang, S. H.; Li, Y. W.; Kawazoe, Y.; Sun, Q.; Jena, P. Structures and Phase Transition of a MoS<sub>2</sub> Monolayer. *J. Phys. Chem. C* **2014**, *118* (3), 1515–1522.
- (7) Benavente, E.; Santa Ana, M.; Mendizabal, F.; Gonzalez, G. Intercalation Chemistry of Molybdenum Disulfide. *Coord. Chem. Rev.* **2002**, *224*, 87–109.
- (8) Pecoraro, T. A.; Chianelli, R. R. Hydrodesulfurization Catalysis by Transition Metal Sulfides. *J. Catal.* **1981**, *67* (2), 430–445.
- (9) Xiang, Q.; Yu, J.; Jaroniec, M. Synergetic Effect of MoS<sub>2</sub> and Graphene as Cocatalysts for Enhanced Photocatalytic H<sub>2</sub> Production Activity of TiO<sub>2</sub> Nanoparticles. *J. Am. Chem. Soc.* **2012**, *134* (15), 6575–6578.
- (10) Wang, H.; Lu, Z.; Xu, S.; Kong, D.; Cha, J. J.; Zheng, G.; Hsu, P.-C.; Yan, K.; Bradshaw, D.; Prinz, F. B.; et al. Electrochemical Tuning of Vertically Aligned MoS<sub>2</sub> Nanofilms and Its Application in Improving Hydrogen Evolution Reaction. *Proc. Natl. Acad. Sci. U. S. A.* **2013**, *110* (49), 19701–19706.
- (11) Kong, D.; Wang, H.; Cha, J. J.; Pasta, M.; Koski, K. K. J.; Yao, J.; Cui, Y. Synthesis of MoS<sub>2</sub> and MoSe<sub>2</sub> Films with Vertically Aligned Layers. *Nano Lett.* **2013**, *13* (3), 1341–1347.
- (12) Kibsgaard, J.; Chen, Z.; Reinecke, B. N.; Jaramillo, T. F. Engineering the Surface Structure of MoS<sub>2</sub> to Preferentially Expose Active Edge Sites for Electrocatalysis. *Nat. Mater.* **2012**, *11* (11), 963–969.
- (13) Li, Y.; Wang, H.; Xie, L.; Liang, Y.; Hong, G.; Dai, H. MoS<sub>2</sub> Nanoparticles Grown on Graphene: An Advanced Catalyst for the Hydrogen Evolution Reaction. *J. Am. Chem. Soc.* **2011**, *133* (19), 7296–7299.
- (14) Jaramillo, T. F.; Jørgensen, K. P.; Bonde, J.; Nielsen, J. H.; Horch, S.; Chorkendorff, I. Identification of Active Edge Sites for Electrochemical H<sub>2</sub> Evolution from MoS<sub>2</sub> Nanocatalysts. *Science* **2007**, *317* (5834), 100–102.
- (15) Lukowski, M. a; Daniel, A. S.; Meng, F.; Forticaux, A.; Li, L.; Jin, S. Enhanced Hydrogen Evolution Catalysis from Chemically Exfoliated Metallic MoS<sub>2</sub> Nanosheets. *J. Am. Chem. Soc.* **2013**, *135* (28), 10274–10277.
- (16) Voiry, D.; Yamaguchi, H.; Li, J.; Silva, R.; Alves, D. C. B.; Fujita, T.; Chen, M.; Asefa, T.; Shenoy, V. B.; Eda, G.; et al. Enhanced Catalytic Activity in Strained Chemically Exfoliated WS<sub>2</sub> Nanosheets for Hydrogen Evolution. *Nat. Mater.* **2013**, *12* (9), 850–855.
- (17) Eda, G.; Fujita, T.; Yamaguchi, H.; Voiry, D.; Chen, M.; Chhowalla, M. Coherent Atomic and Electronic Heterostructures of Single-Layer MoS<sub>2</sub>. *ACS Nano* **2012**, *6* (8), 7311–7317.
- (18) Lin, Y.-C.; Dumcenco, D. O.; Huang, Y.-S.; Suenaga, K. Atomic Mechanism of the Semiconducting-to-Metallic Phase Transition in Single-Layered MoS<sub>2</sub>. *Nat. Nanotechnol.* **2014**, *9* (5), 391–396.
- (19) Kapper, R.; Voiry, D.; Yalcin, S. E. S.; Branch, B.; Gupta, G.; Mohite, A. D.; Chhowalla, M. Phase-Engineered Low-Resistance Contacts for Ultrathin MoS<sub>2</sub> Transistors. *Nat. Mater.* **2014**, *13* (12), 1128–1134.
- (20) Qin, X.; Yang, D.; Frindt, R.; Irwin, J. Real-Space Imaging of Single-Layer MoS<sub>2</sub> by Scanning Tunneling Microscopy. *Phys. Rev. B: Condens. Matter Mater. Phys.* **1991**, *44* (7), 3490–3493.
- (21) Jimenez Sandoval, S.; Yang, D.; Frindt, R.; Irwin, J. Raman Study and Lattice Dynamics of Single Molecular Layers of MoS<sub>2</sub>. *Phys. Rev. B: Condens. Matter Mater. Phys.* **1991**, *44* (8), 3955–3962.
- (22) Dines, M. B. LITHIUM INTERCALATION via N-BUTYLLITHIUM OF THE LAYERED TRANSITION METAL DICHALCOGENIDES. *Mater. Res. Bull.* **1975**, *10*, 287–292.
- (23) Kresse, G.; Furthmüller, J. Efficient Iterative Schemes for Ab Initio Total-Energy Calculations Using a Plane-Wave Basis Set. *Phys. Rev. B: Condens. Matter Mater. Phys.* **1996**, *54* (16), 11169–11186.
- (24) Sheppard, D.; Xiao, P.; Chemelewski, W.; Johnson, D. D.; Henkelman, G. A Generalized Solid-State Nudged Elastic Band Method. *J. Chem. Phys.* **2012**, *136* (7), 074103.
- (25) Lee, C.; Yan, H.; Brus, L.; Heinz, T.; Hone, J.; Ryu, S. Anomalous Lattice Vibrations of Single- and Few-Layer MoS<sub>2</sub>. *ACS Nano* **2010**, *4* (5), 2695–2700.
- (26) Liang, L.; Meunier, V. First-Principles Raman Spectra of MoS<sub>2</sub>, WS<sub>2</sub> and Their Heterostructures. *Nanoscale* **2014**, *6* (10), 5394–5401.
- (27) Frey, G. L.; Tenne, R.; Matthews, M. J.; Dresselhaus, M. S.; Dresselhaus, G. Raman and Resonance Raman Investigation of MoS<sub>2</sub> Nanoparticles. *Phys. Rev. B: Condens. Matter Mater. Phys.* **1999**, *60* (4), 2883–2892.
- (28) Golasa, K.; Grzeszczyk, M.; Leszczyński, P.; Faugeras, C.; Nicolet, A. A. L.; Wyszomolek, A.; Potemski, M.; Babiński, A. Multiphonon Resonant Raman Scattering in MoS<sub>2</sub>. *Appl. Phys. Lett.* **2014**, *104*, 092106.
- (29) Chakraborty, B.; Matte, H. S. S. R.; Sood, A. K.; Rao, C. N. R. Layer-Dependent Resonant Raman Scattering of a Few Layer MoS<sub>2</sub>. *J. Raman Spectrosc.* **2013**, *44* (1), 92–96.
- (30) Livneh, T.; Spanier, J. E. A Comprehensive Spectral Analysis of Multiphonon Resonant Raman Scattering in 2H-MoS<sub>2</sub>. *arXiv: 1408.6748*, 2014.
- (31) Berciaud, S.; Han, M. Y.; Mak, K. F.; Brus, L. E.; Kim, P.; Heinz, T. F. Electron and Optical Phonon Temperatures in Electrically Biased Graphene. *Phys. Rev. Lett.* **2010**, *104* (22), 227401.
- (32) Herman, I. P. Peak Temperatures from Raman Stokes/anti-Stokes Ratios during Laser Heating by a Gaussian Beam. *J. Appl. Phys.* **2011**, *109* (1), 016103.
- (33) Yamamoto, M.; Einstein, T. L.; Fuhrer, M. S.; Cullen, W. G. Anisotropic Etching of Atomically Thin MoS<sub>2</sub>. *J. Phys. Chem. C* **2013**, *117* (48), 25643–25649.
- (34) Lavik, M. T.; Medved, T. M.; Moore, G. D. Oxidation Characteristics of MoS<sub>2</sub> and Other Solid Lubricants. *ASLE Trans.* **1968**, *11* (1), 44–55.
- (35) Tsai, H.-L.; Heising, J.; Schindler, J. L.; Kannewurf, C. R.; Kanatzidis, M. G. Exfoliated–Restacked Phase of WS<sub>2</sub>. *Chem. Mater.* **1997**, *9* (4), 879–882.
- (36) Brus, L. E.; Harkless, J. A. W.; Stilling, F. H. Theoretical Metastability of Semiconductor Crystallites in High-Pressure Phases,

with Application to B-Tin Structure Silicon. *J. Am. Chem. Soc.* **1996**, *118* (20), 4834–4838.

(37) Wypych, F.; Schollhorn, R. 1T-MoS<sub>2</sub>, a New Metallic Modification of Molybdenum Disulfide. *J. Chem. Soc., Chem. Commun.* **1992**, *19*, 1386–1388.

(38) Liu, L.; Park, J.; Siegel, D. A.; McCarty, K. F.; Clark, K. W.; Deng, W.; Basile, L.; Idrobo, J. C.; Li, A.-P.; Gu, G. Heteroepitaxial Growth of Two-Dimensional Hexagonal Boron Nitride Templated by Graphene Edges. *Science* **2014**, *343* (6167), 163–167.

(39) Siegal, Y.; Glezer, E. N.; Huang, L.; Mazur, E. Laser-Induced Phase Transitions in Semiconductors. *Annu. Rev. Mater. Sci.* **1995**, *25* (1), 223–247.

(40) Callan, J. P.; Kim, A. M.-T.; Roeser, C. A. D.; Mazur, E.; Solis, J.; Siegel, J.; Afonso, C. N.; de Sande, J. C. G. Ultrafast Laser-Induced Phase Transitions in Amorphous GeSb Films. *Phys. Rev. Lett.* **2001**, *86* (16), 3650–3653.

(41) Kitagawa, R.; Takebe, H.; Morinaga, K. Photoinduced Phase Transition of Metallic SmS Thin Films by a Femtosecond Laser. *Appl. Phys. Lett.* **2003**, *82* (21), 3641.